Volume 12
Number 27
21 July 2021
Pages 9249–9562

Chemical Science

rsc.li/chemical-science

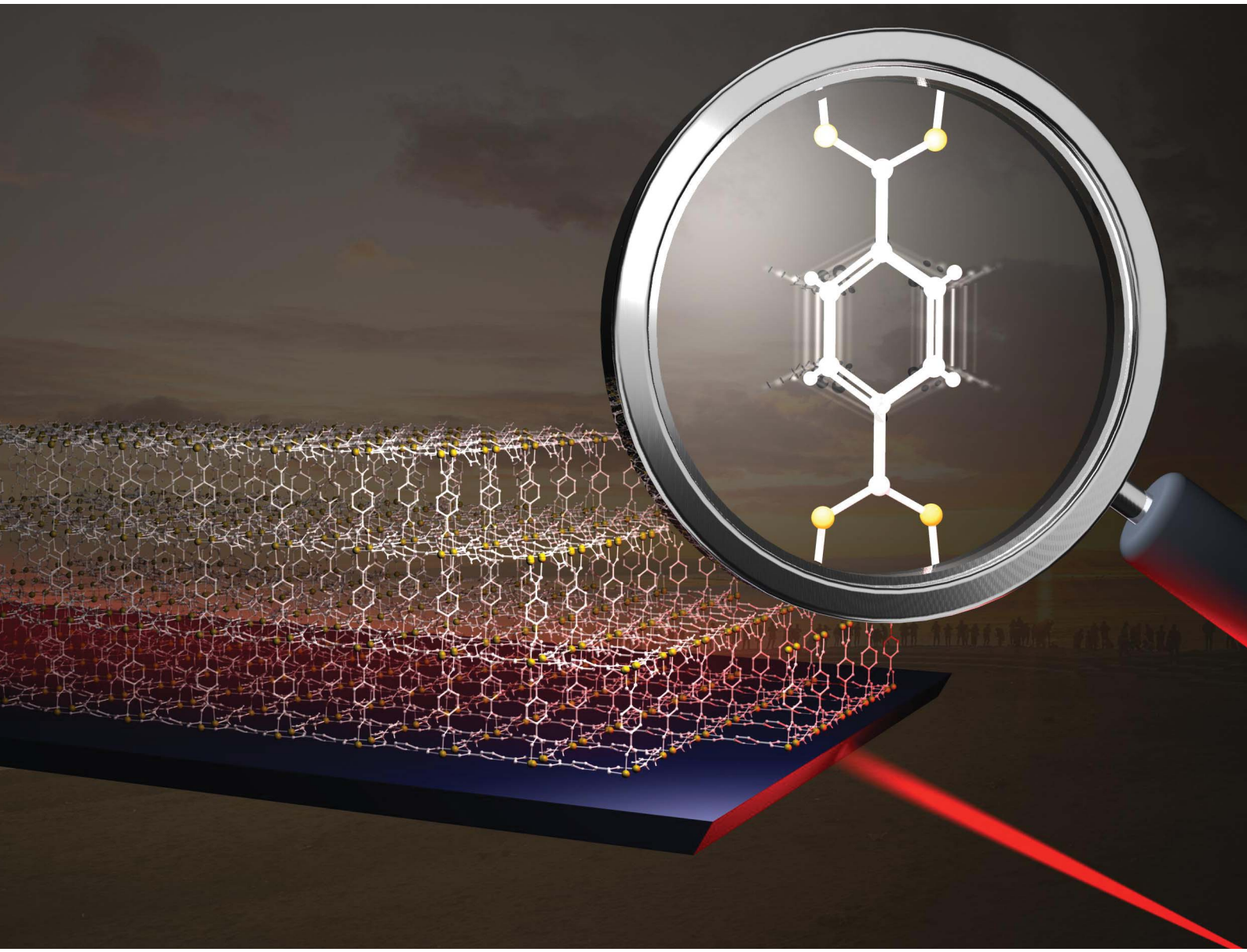

ISSN 2041-6539

ROYAL SOCIETY OF CHEMISTRY

EDGE ARTICLE
Kenji Okada, Masahide Takahashi *et al.*
Infrared crystallography for framework and linker orientation in metal–organic framework films

Chemical Science

ROYAL SOCIETY OF CHEMISTRY

EDGE ARTICLE

View Article Online
View Journal | View Issue

Check for updates

Cite this: *Chem. Sci.*, 2021, **12**, 9298

All publication charges for this article have been paid for by the Royal Society of Chemistry

Infrared crystallography for framework and linker orientation in metal–organic framework films†

Bettina Baumgartner,[a] Ken Ikigaki,[a] Kenji Okada *[ab] and Masahide Takahashi *[a]

Pore alignment and linker orientation influence diffusion and guest molecule interactions in metal–organic frameworks (MOFs) and play a pivotal role for successful utilization of MOFs. The crystallographic orientation and the degree of orientation of MOF films are generally determined using X-ray diffraction. However, diffraction methods reach their limit when it comes to very thin films, identification of chemical connectivity or the orientation of organic functional groups in MOFs. Cu-based 2D MOF and 3D MOF films prepared *via* layer-by-layer method and from aligned $Cu(OH)_2$ substrates were studied with polarization-dependent Fourier-transform infrared (FTIR) spectroscopy in transmission and attenuated total reflection configuration. Thereby, the degrees for in-plane and out-of-plane orientation, the aromatic linker orientation and the initial alignment during layer-by-layer MOF growth, which is impossible to investigate by laboratory XRD equipment, was determined. Experimental IR spectra correlate with theoretical explanations, paving the way to expand the principle of IR crystallography to oriented, organic–inorganic hybrid films beyond MOFs.

Received 28th April 2021
Accepted 7th June 2021

DOI: 10.1039/d1sc02370e

rsc.li/chemical-science

Introduction

In metal–organic frameworks (MOFs), organic linkers and metal-containing units are combined, forming porous materials with great variety and multiplicity regarding constituents' geometry, pore size and functionality.[1] Their fields of applications are equally manifold and include photonics,[2] energy-related applications such as solar or fuel cells,[3,4] homogeneous and heterogeneous catalysis,[5,6] gas and fuel storage,[7,8] or (bio-)sensing.[9–11] While MOFs are available in a great variety of shapes, such as nanocrystals, nanospheres, or hierarchical monoliths, MOF thin films hold tremendous potential to translate the structural properties of individual crystals to continuous, scalable materials. Scalability and processability are essential for the application of MOFs in numerous fields[12,13] such as optics,[9] photonics,[2] catalytic coatings, sensing, solar cells or for batteries.[14] The majority of these applications rely on the precise crystallographic orientation and uniform porosity of the MOF to allow for *e.g.* electron- or photoconduction. Hence, controlling and determining the crystallinity and orientation, including framework and linker orientation, of the MOF film with respect to the substrate is of prime importance for successful implementations.

Typically, oriented MOF thin films are synthesized by the layer-by-layer (LbL) approach on substrates modified with self-assembled monolayers (SAM).[15] Thereby, MOF films composed of 2D sheets (2D MOF) and coordinatively connected 2D sheets by pillar molecules (3D MOFs) with a multitude of different organic and metallic building blocks have been obtained.[16–18] Although, this method allows to control the orientation of the lattice plane parallel to the substrate (out-of-plane orientation) by changing the terminated functional group of the SAM, these MOF films lack in-plane orientation.[19] Recently, our group reported a synthetic method to obtain three-dimensionally oriented 2D and 3D Cu-based MOF films by epitaxial growth on copper hydroxide,[20,21] yielding large scale films with controlled pore alignment.

The standard method to determine the crystallographic orientation, and thus the pore alignment, of MOF films is X-ray diffraction (XRD) in out-of-plane (OOP) and in-plane (IP) configuration, *i.e.* perpendicular and horizontal relative to the substrate. The degree of in-plane orientation of films can be quantified using azimuthal angle dependent intensity profiles (φ scan) in the in-plane XRD configuration, *i.e.* rotating the sample around the axis perpendicular to the substrate center (φ axis) at constant X-ray source and detector position.[20–22] Besides dedicated diffractometer equipment and rather long measurement times of several hours, this method requires for considerably thick MOF films (typically >40 layers of LbL MOF films) to achieve sufficient signal-to-noise ratios.

With respect to high surface sensitivity, infrared reflection absorption spectroscopy (IRRAS) has proven as powerful tool to

[a]*Department of Materials Science, Graduate School of Engineering, Osaka Prefecture University, Sakai, Osaka, 599-8531, Japan*

[b]*JST, PRESTO, 4-1-8 Honcho, Kawaguchi, Saitama 332-0012, Japan. E-mail: k_okada@mtr.osakafu-u.ac.jp; masa@mtr.osakafu-u.ac.jp*

† Electronic supplementary information (ESI) available. See DOI: 10.1039/d1sc02370e

determine the structure and orientation of molecular layers on planar surfaces,[23,24] to study the initial growth of MOF films,[25] or determine structural defects within MOF films.[26,27] Polarized IR radiation is reflected from a thin film deposited on metallic surfaces under a grazing angle of incidence. In this configuration, parallel-polarized light is solely absorbed by molecules with chemical bands having their transition dipole moment perpendicular to the substrate's surface.[28,29] Thus, IRRAS provides structural, chemical information on the axis perpendicular to the surface. This fact has been exploited by Terfort and co-works to differentiate between surface-attached MOF (SURMOF) films synthesized in different crystallographic orientations.[19,30] The carboxylate bands originating from the coordination of the organic linker with the metal nodes are ideally suited to study the MOF orientation: four carboxylate bonds in their bridging configuration are oriented in a Cu-paddle wheel that directs the structure of all MOFs with bimetal building units (*e.g.* MOFs based on M = Cu, Cr, Mo, *etc.*, compare Fig. 1).[31] The perpendicular orientation of the carboxylate bonds to each other and also to the surface allowed Terfort and co-works to determine the out-of-plane orientation of MOF films with different preferred orientation synthesized by LbL synthesis on gold surfaces functionalized with SAMs.[19,30] Although IRRAS is well suited to study MOF films prepared from SAMs, the technique is restricted to oriented films deposited on metal surfaces. Furthermore, information on the orientation of chemical bonds apart from perpendicular orientation, *i.e.* out-of-plane, is not accessible.

Polarization-dependent IR spectroscopy in transmission and attenuated total reflection (ATR) geometry is highly sensitive to structural changes and atomic interactions in *x*, *y* and *x*, *y*, *z*-direction (*i.e.* in-plane and out-of-plane, compare Fig. 1), respectively. Researchers mainly in the fields of macromolecular chemistry and structural biology have taken advantage of these sensitivity to study the degree of crystallinity and the orientation in (semi-)crystalline polymers[32–34] or the conformational changes in biomolecules.[35–37] In this context, the term *infrared crystallography* is commonly used, even though the method only provides information on the orientation of molecules and functional groups but not the crystal's periodicity.[36]

In this contribution, as outlined in Fig. 1, we employed polarization-dependent IR spectroscopy to study the in-plane and out-of-plane orientation of Cu-based 2D and 3D MOF films on Si substrates. Besides confirming the film orientation and comparing favorably with results from XRD measurements just obtained at shorter time scales, additional structural information was retrieved: the orientation of the aromatic linker in the 3D MOF $Cu_2(BDC)_2DABCO$ (BDC: 1,4-benzenedicarboxylate, DABCO: 1,4-diazabicyclo[2.2.2]octane), to date inaccessible with conventional techniques such as XRD and IRRAS, and highly essential for the accessibility of the pores, was determined to be parallel to the 2D MOF sheets and perpendicular to the bridging carboxylate plane. Furthermore, the initial orientation of MOF films in the LbL synthesis, otherwise only feasible with synchrotron techniques due to the low amount of material, could be investigated.

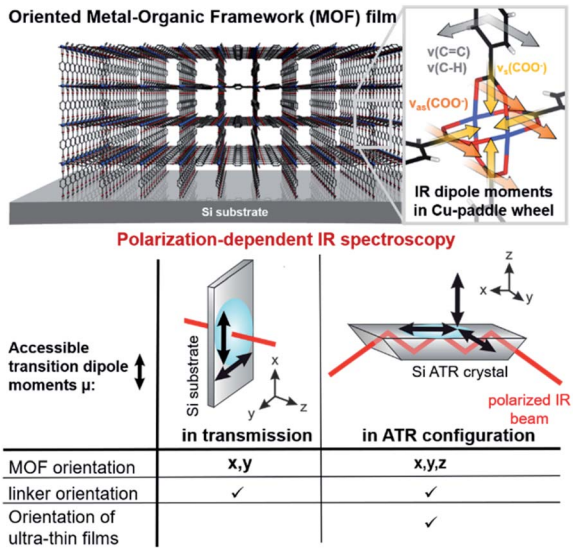

Fig. 1 Cu-paddle wheel structure within an oriented MOF film. Transition dipole moments of the IR vibrations of the carboxylate and the aromatic ring present in the MOF are indicated with arrows. Schematic of IR spectroscopy in transmission and ATR configuration for thin film analysis and accessible transition dipole moments with respect to the surface.

Results and discussion

Degree of in-plane orientation from polarization-dependent IR spectroscopy in transmission

Oriented CuBDC and $Cu_2(1,4\text{-NDC})_2DABCO$ (1,4-NDC: 1,4-naphthalenedicarboxylate) films were grown from $Cu(OH)_2$ nanobelt films *via* a heteroepitaxial growth approach.[20,21] MOF films with high and low degrees of in-plane orientation were prepared on silicon substrates from aligned and randomly aligned $Cu(OH)_2$ nanobelt films (see ESI† for $Cu(OH)_2$ preparation and characterization). The corresponding SEM images and XRD patterns are given in Fig. 2. SEM observation indicates that MOF crystals grown from oriented $Cu(OH)_2$ nanobelts are oriented in three dimensions (*x*, *y* and *z* direction), while randomly oriented $Cu(OH)_2$ nanobelts yield MOF crystals only oriented perpendicular to the surface (*z*-direction) without in-plane orientation. This conclusion drawn from MOF morphologies in the SEM images was further confirmed with XRD. For MOF thin films prepared from randomly oriented $Cu(OH)_2$, there is a clear difference between out-of-plane and in-plane XRD patterns, but no difference is observed between the two types of in-plane XRD patterns, confirming that the CuBDC and $Cu_2(1,4\text{-NDC})_2DABCO$ MOF films have only out-of-orientation as reported previously.[38,39] In contrast, MOF films prepared from oriented $Cu(OH)_2$ nanobelt films show strong dependence on X-ray incidence angle as visible in the IP XRD patterns, confirming the fabrication of three-dimensionally oriented MOF films. Collectively, in MOF thin films synthesized from oriented $Cu(OH)_2$, the *c* axis in CuBDC and *b* axis in $Cu_2(1,4\text{-NDC})_2DABCO$ are along the *z*-direction and the *b* axis in CuBDC and *c* axis in $Cu_2(1,4\text{-NDC})_2DABCO$ are parallel to the longitudinal direction (*y*-direction) of the underlying $Cu(OH)_2$

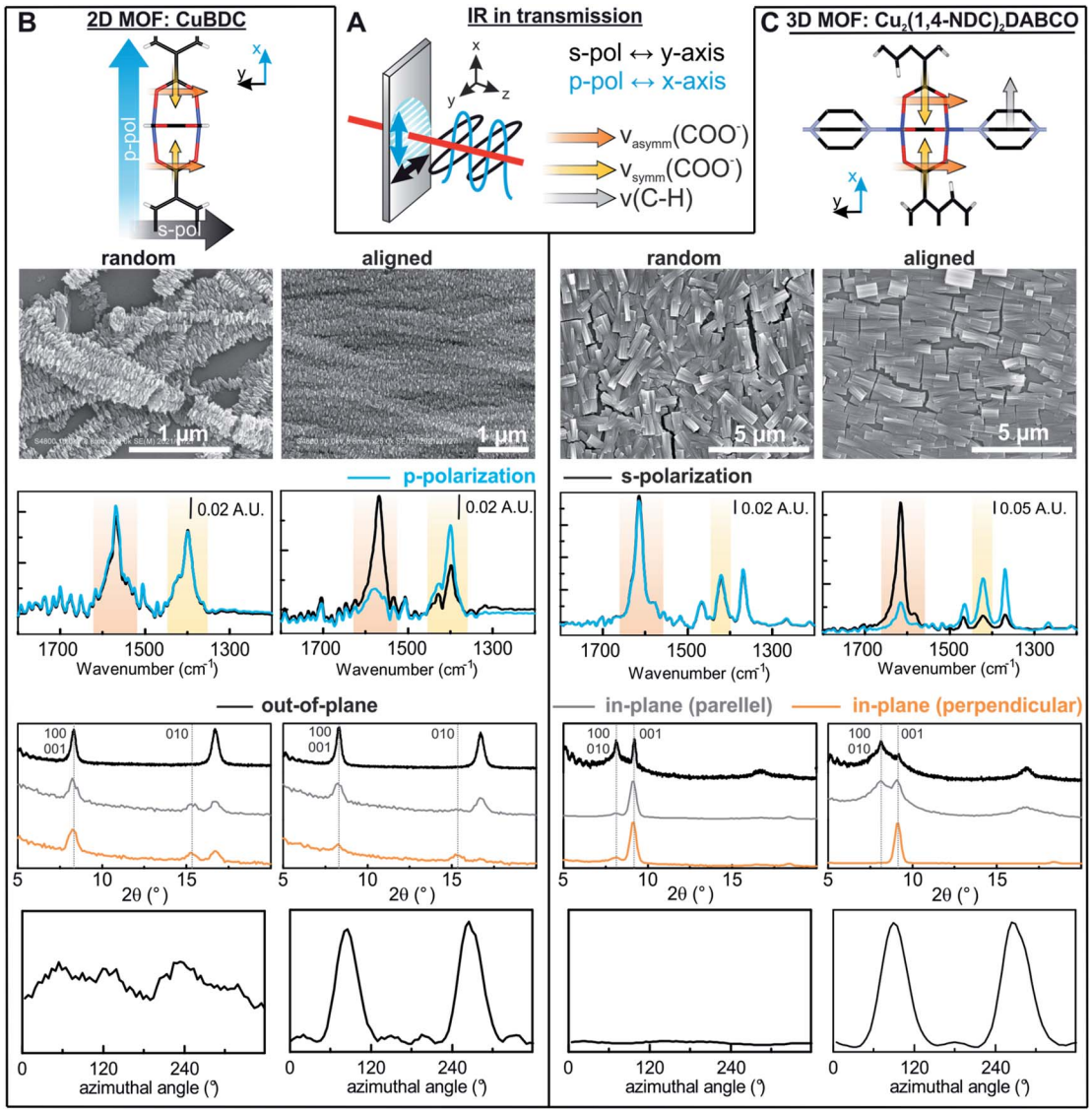

Fig. 2 (A) Schematic representation of a MOF film on Si substrate studied in transmission configuration using polarized IR light. Orientation of the long axis of the $Cu(OH)_2$ nanobelts is indicated with white lines. (B) and (C) Cu-paddle wheel units in CuBDC (B) and Cu_2(1,4-NDC)$_2$DABCO (C) with respect to the polarization of the incident light. Transition dipole of symmetric and asymmetric carboxylate vibrations are highlighted in yellow and orange, respectively. Atom color code: C: black, H: white, Cu: blue, N: lilac, O: red. CuBDC and Cu_2(1,4-NDC)$_2$DABCO films obtained from random and aligned $Cu(OH)_2$ nanobelts and corresponding SEM images, and polarized IR transmission spectra. $\nu_{asymm}(COO^-)$ bands are highlighted in orange, while the bands corresponding to the $\nu_{symm}(COO^-)$ band are highlighted in yellow. XRD patterns in out-of-plane (black lines) and in-plane configurations (gray and orange lines, where the X-ray incident angle is parallel and perpendicular to the longitudinal direction of the nanobelts at $2\theta = 0°$): reflections originated from MOFs are indicated. φ scans were recorded for the 100 reflection for CuBDC and for the 001 reflection for Cu_2(1,4-NDC)$_2$DABCO. For comparability, φ-scans for random and aligned MOF films are given for the same scale on the y-axis for each MOF pair.

nanobelts (see Fig. S4† for visualization of MOF film structures). This alignment was further quantified by φ scan measurements, which are given in Fig. 2.

From these profiles, the degree of in-plane orientation was determined using the full width at half maximum (FWHM) of the peaks and eqn (1):[40]

$$F_{XRD} = \frac{180° - \text{FWHM}}{180°} \quad (1)$$

yielding $F_{XRD} = 0.80$ and 0.82 for aligned CuBDC and Cu_2(1,4-NDC)$_2$DABCO films, respectively. MOF films from randomly aligned $Cu(OH)_2$ nanobelts show only broad signals in the φ scan as expected.

FTIR spectra recorded with s- and p-polarized light of the same set of films with different degrees of orientation were acquired in transmission using blank silicon as background and are given in Fig. 2 The bands at 1570 cm^{-1} and 1616 cm^{-1} stem from the asymmetric carboxylate vibration, and the bands at 1390 cm^{-1} and 1423 cm^{-1} are assigned to the symmetric carboxylate vibration, which is consistent with previous reports.[39,41] The bands at 1465 and 1370 cm^{-1} in the 3D MOF stem from C–H vibrations of DABCO with a transition dipole

moment perpendicular to the N–N axis.[42] No spectral differences between the polarized IR spectra were observed for the MOF films obtained from random $Cu(OH)_2$ nanobelts, while a strong polarization-dependence is visible for three-dimensionally oriented MOF films.

The reason for this becomes clear if we set the orientation of the Cu-paddle wheel of CuBDC and Cu_2(1,4-NDC)$_2$DABCO in relation to the Si substrate as given in Fig. 2A: the transition dipole of the $\nu_{symm}(COO^-)$ band (yellow arrow) is oriented in *x*-direction, thus, this band can only interact with p-polarized light. *Vice versa* holds true for the asymmetric vibration that can only interact with s-polarized light. This polarization dependence is visible in the spectra of both aligned films. Furthermore, the transition dipole moments of the C–H vibrations of DABCO present in the 3D MOFs are oriented in *x*-direction and hence show the same polarization-dependence as the equally oriented dipole of the $\nu_{symm}(COO^-)$ band. Note that, even if DABCO can rotate freely around the N–N axis, this would not change the fact that it C–H groups only interacts with p-polarized light. For a perfectly aligned film, no bands for the symmetric and asymmetric vibration would be visible for p- and s-polarized light, respectively. However, the investigated MOF films show a degree of in-plane orientation of 0.80 and 0.82 determined from XRD data, respectively, hence, misaligned crystallites are present. This misalignment leads to vibrations of $\nu_{symm}(COO^-)$ in the s-polarized spectrum and $\nu_{asymm}(COO^-)$ in the p-polarized spectrum. This fact allows to use the linear dichroism, *i.e.* the ratio of absorbance for s- and p-polarization, of each COO^- vibration to calculate the degree of in-plane orientation F_{IR} from IR transmission spectra. The respective band areas A were integrated, and F_{IR} was retrieved using the following equations:

$$F_{IR}\left(\nu_{asym}(COO^-)\right) = \frac{A_{\nu_{asymm}(COO^-),\parallel}}{A_{\nu_{asymm}(COO^-),\perp} + A_{\nu_{aysmm}(COO^-),\parallel}} \quad (2)$$

$$F_{IR}\left(\nu_{sym}(COO^-)\right) = \frac{A_{\nu_{symm}(COO^-),\perp}}{A_{\nu_{symm}(COO^-),\perp} + A_{\nu_{symm}(COO^-),\parallel}} \quad (3)$$

Thereby, $F_{IR}(\nu_{asymm}(COO^-))$ values of 0.80 and 0.80 were obtained from the spectra of both aligned MOF films in Fig. 2, which is in excellent agreement with the degree of orientation obtained from XRD experiment. $F_{IR}(\nu_{symm}(COO^-)) = 0.68$ for CuBDC, which has less correlation with the corresponding F_{XRD} value. We attribute this deviation of F_{IR} to F_{XRD} to crystallite tilting and a different structure, as we will discuss in the last section.

To demonstrate that this method is valid over the entire range of in-plane orientation values, we prepared CuBDC and Cu_2(1,4-NDC)$_2$DABCO films from $Cu(OH)_2$ films with different degrees of orientation. The in-plane orientation of all films was determined with φ-scans in XRD and FTIR transmission spectroscopy. The results are compared in Fig. 3 and show similar values for F_{IR} values >0.5. A lower correlation was found for the $\nu_{symm}(COO^-)$ band for CuBDC. Note that $F_{IR} = 0.5$ corresponds to completely unoriented films, while $F_{IR} = 0$ results only from films perfectly aligned perpendicular to films with $F_{IR} = 1$ (see

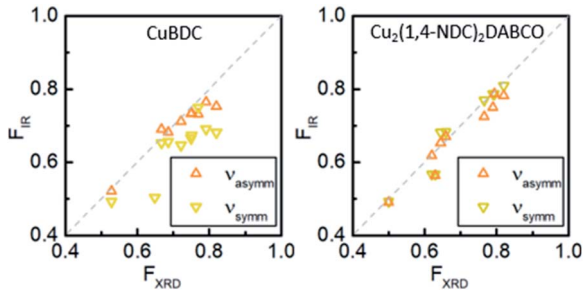

Fig. 3 Correlation of degree of orientation *F* obtained from XRD and FTIR spectroscopy in transmission for CuBDC and Cu_2(1,4-NDC)$_2$-DABCO films for $\nu_{symm}(COO^-)$ and $\nu_{asymm}(COO^-)$ bands.

Fig. S6 in ESI† for graphical illustration). In contrast, F_{XRD} is an arbitrarily defined ratio that allows comparison between oriented films.[40] In addition, peak fitting and determining the FWHM becomes increasingly prone to errors for $F_{XRD} < 0.5$ and yields $-\infty$ for films without preferential orientation and flat φ-scans. For these reasons, a correlation between F_{IR} and F_{XRD} is physically not valid and shall only be used to compare films during material development for $F > 0.5$. Nevertheless, these findings show that the degree of in-plane orientation of 2D and 3D MOF films in the given boarders can be derived from simple FTIR transmission spectra on Si substrates, which allows for fast screening without the need of dedicated diffraction instrumentation or substrates with metallic coatings.

Crystallographic orientation of MOF films in all three axes studied with ATR spectroscopy

In contrast to spectra acquired in transmission, ATR spectroscopy provides two advantages: (i) higher interaction path-lengths, and hence higher sensitivity, can be achieved with multibounce ATR crystals, as used in this study; and (ii) ATR spectroscopy gives access to all three axes of the studied materials. This is due to the fact that the evanescent wave generated upon total reflection at the ATR crystal/sample interface has fractions of the field amplitude in all directions, namely E_x, E_y, E_z, which are polarization-dependent: s-polarized light only generates an evanescent wave in *y*-direction, while p-polarized light induces an evanescent wave in *x* and *z*-direction (compare Fig. 4). E_x, E_y, E_z are not equal in amplitude and depend on the refractive index of sample and ATR crystal material, n_2 and n_1, respectively, and the angle of incidence θ. The fractions of the field amplitudes at the ATR crystal's ($z = 0$) surface can be determined using eqn (4)–(6):[43]

$$E_{y,0} = \frac{2i\cos\theta}{\left(1 - \frac{1}{\varepsilon}\right)^{\frac{1}{2}}} \quad (4)$$

$$E_{x,0} = 2\cos(\theta)\left(\frac{\sin^2\theta - \frac{1}{\varepsilon}}{\sin^2\theta - \frac{1}{\varepsilon} + \frac{\cos^2\theta}{\varepsilon^2}}\right)^{\frac{1}{2}} \quad (5)$$

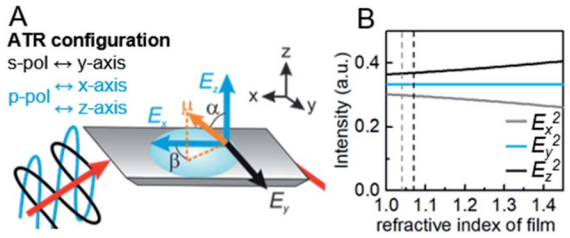

Fig. 4 (A) Linearly polarized light entering a trapezoidal Si ATR crystal coated with a MOF film at an angle of incidence θ. Total reflection of s-polarized light causes an evanescent wave amplitude E_y, while p-polarized light generates E_x and E_z. (B) Fractions of E_x^2, E_y^2 and E_z^2 as function of the refractive index of the MOF film for Si ATR crystals with $\theta = 45°$. Effective refractive indices $n_{2,\text{effective}}$ of CuBDC and Cu_2(1,4-NDC)$_2$DABCO films are indicated by gray and black dashed lines, respectively.

$$E_{z,0} = \frac{2i \sin\theta \cos\theta}{\varepsilon\left[\sin^2\theta - \frac{1}{\varepsilon} + \frac{\cos^2\theta}{\varepsilon^2}\right]^{\frac{1}{2}}} \quad (6)$$

with $\varepsilon = (n_1/n_2)^2$. The polarization dependent absorbance $A_{\parallel}$ and $A_{\perp}$ is proportional to the evanescent wave, the transition dipole vector of the vibration in question and the angle between both vectors (compare Fig. 4):[44,45]

$$A_{\perp} \propto (\mu_y E_y)^2 = (\mu_0 \sin\alpha \sin\beta E_y)^2 \quad (7a)$$

$$A_{\parallel} \propto (\mu_x E_x)^2 + (\mu_z E_z)^2 = (\mu_0 \sin\alpha \cos\beta E_x)^2 + (\mu_0 \cos\alpha E_z)^2 \quad (7b)$$

The simplified eqn (7a) and (7b) hold true for MOFs with the molecule axis aligned along the coordination system of the ATR crystal, as in the case for the studied MOF films (see ref. 44 and 45 for more complex systems), and only for aligned dipoles, not for dipole distributions. The $\nu_{\text{symm}}(COO^-)$ and $\nu_{\text{asymm}}(COO^-)$ bands in the films investigated have dipole moments with a and $ß$ being either 0° or 90°, which simplifies interpretation of polarization dependent spectra. However, the trigonometric relationship allows also to study bands under a specific angle.

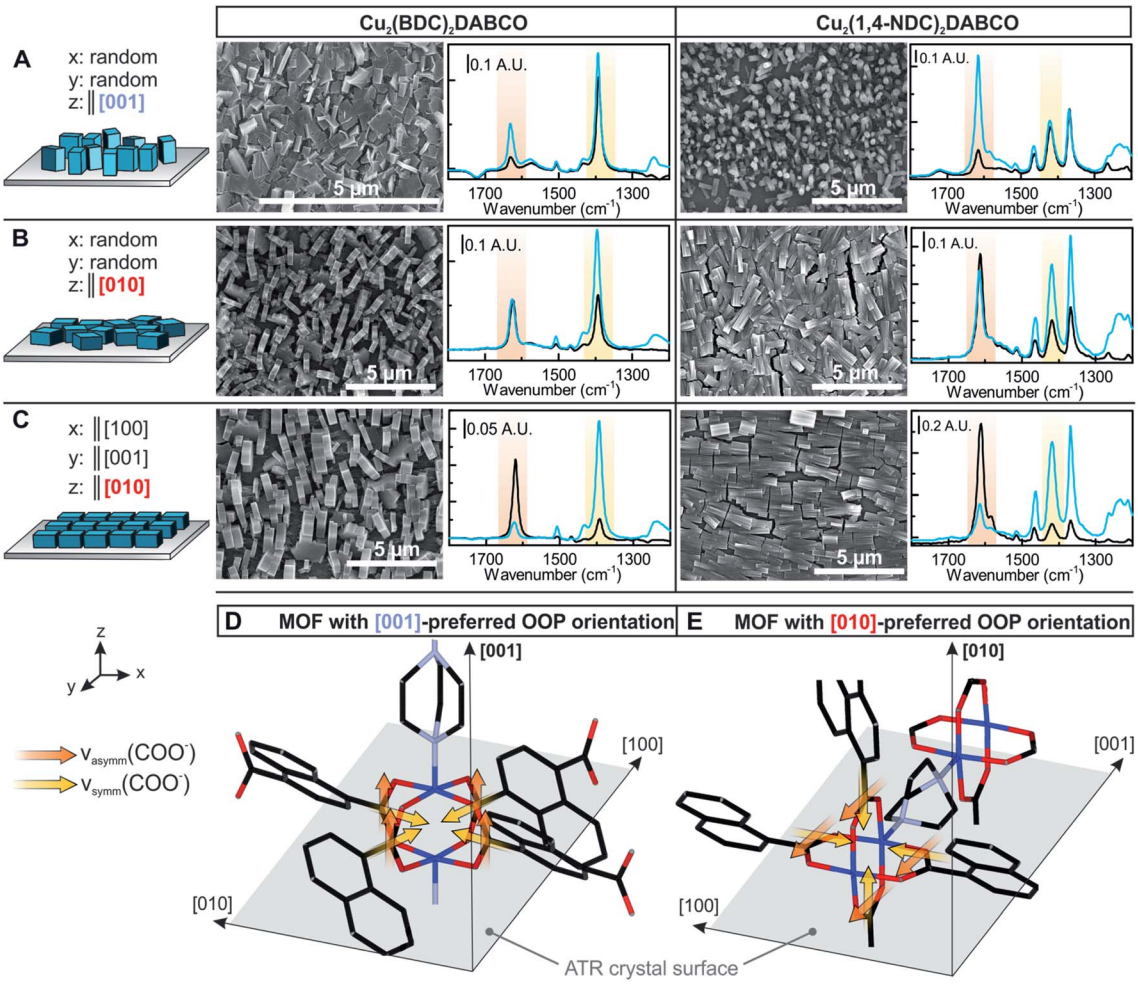

Fig. 5 Cu_2(BDC)$_2$DABCO and Cu_2(1,4-NDC)$_2$DABCO in different crystallographic orientation with respect to the Si ATR crystal's surface: IR spectra (p-polarized spectrum = blue, s-polarized spectrum = black) of MOF films with z‖[001] (A row) show polarization-dependence for the $\nu_{\text{asymm}}(COO^-)$ band, while equal absorbance is visible for the $\nu_{\text{symm}}(COO^-)$ band (compare D). IR spectra of MOF films with z‖[010] show polarization-dependent $\nu_{\text{symm}}(COO^-)$ bands for MOFs only aligned in z-direction (B row), while both COO^- bands are affected for MOF films oriented in x, y, z direction (C row and compare E). Background of IR spectra = blank silicon ATR crystal.

The ratio of absorbances $A_{\parallel}$ and A_{normal} measured for p-polarized and s-polarized light, respectively, is called the dichroic ratio R:

$$R = \frac{E_x^{\,2} + E_z^{\,2}}{E_y^{\,2}} = \frac{A_{\parallel}}{A_{\perp}} \tag{8}$$

Experimentally, R can be determined by comparing the absorbance of a specific band in both polarizations. $R = 2$ for an angle of incidence of 45° (as used in this study) and isotropic bulk samples such as water (see Fig. S9† for spectra). Note that R is unity for isotropic media investigated in transmission. The calculated field amplitudes for varying refractive indices of the sample are depicted in Fig. 4 (see ESI† for further information). The fraction of E_y remains constant, while E_x and E_z are affected by the refractive index of the sample (see ESI† for further information on the determination of the refractive index of the films). With the relative intensities of the evanescent wave in each direction of $E_x^{\,2} = 0.30$, $E_y^{\,2} = 0.33$, $E_z^{\,2} = 0.37$ at hand, the orientation of MOF films can be determined. 3D MOFs with different crystallographic orientation were prepared on Si ATR crystals and the SEM images of the films and corresponding ATR-IR spectra of $Cu_2(BDC)_2DABCO$ and $Cu_2(1,4\text{-}NDC)_2DABCO$ films are given in Fig. 5. Their crystallographic orientations were confirmed by XRD (see Fig. S10 in ESI†) and the orientation of the MOFs in x, y and z-direction is shown schematically on the left in Fig. 5.

The Cu–Cu axis of Cu-paddle wheel unit and the N–N axis of the DABCO pillar are oriented perpendicular to the substrate in 3D MOF films with [001] preferred OOP orientation (compare Fig. 5D). Both MOF films with [001] preferred OOP orientation show no in-plane orientation (Fig. 5A). This gives rise to transition dipole moments of the $\nu_{\text{asymm}}(COO^-)$ bands oriented in z-direction, while the dipole moments of the $\nu_{\text{symm}}(COO^-)$ band are aligned in the x–y plane, which is consistent with the recorded IR spectra: $\nu_{\text{asymm}}(COO^-)$ is only visible in the p-polarized spectrum and only contributions of MOF crystallites deviating from the z-axis alignment contribute to this band in the s-polarized spectrum (compare Table 1 for R values). As MOF films with [001] preferred OOP orientation rotate freely around the z-axis and due to the fact that both $\nu_{\text{symm}}(COO^-)$ and ν_{symm}(C–H) are oriented in the x–y plane, these bands show the same absorbance for both polarizations. Two types of MOFs films with [010] preferred OOP orientation (compare Fig. 5E) were prepared from random and aligned $Cu(OH)_2$ nanobelts, yielding MOFs films with and without in-plane orientation (Fig. 5B and C). For 3D MOFs prepared from randomly oriented $Cu(OH)_2$, the transition dipole moment of the $\nu_{\text{asymm}}(COO^-)$ rotates freely around the z-axis, characterized by identical absorbance in p- and s-polarized spectra. For the transition dipole moment of the $\nu_{\text{symm}}(COO^-)$ and of ν(C–H) bands determining the dichroic ratio is more complex as contributions in all three axes have to be considered (see ESI† for full explanation).

A dichroic ratio of 2 was derived for this case as found in the spectra of both 3D MOFs. Lastly, 3D MOF films prepared from oriented $Cu(OH)_2$ nanobelts show a high degree of IP and OOP orientation. The transition dipole moment of the $\nu_{\text{asymm}}(COO^-)$ band is oriented in y-direction, thus yielding absorbance in the s-polarized spectra. The dipole moments of $\nu_{\text{symm}}(COO^-)$ and ν_{symm}(C–H) bands are oriented in x- and z-direction and therefore interact with p-polarized light. Analogous to the previous section, φ scans were recorded and F_{XRD} was determined to be 0.83 and 0.82 for $Cu_2(BDC)_2DABCO$ and $Cu_2(1,4\text{-}NDC)_2DABCO$, respectively. F_{IR} was determined from the ATR spectra (using eqn (2) and (3)) to be 0.84 and 0.83 for $\nu_{\text{symm}}(COO^-)$ band. For aligned films, $F_{\text{IR}}(\nu_{\text{asymm}}(COO^-)) = F_{\text{IR,OOP}}$ and was determined to be 0.83 and 0.82 for the $Cu_2(BDC)_2DABCO$ film and $Cu_2(1,4\text{-}NDC)_2DABCO$ film, respectively.

Note that also transmission IR spectra show distinct differences that can be used to determine the MOF orientation (compare ESI† for explanation). This set of 3D MOF films demonstrates that different crystallographic orientations can be easily distinguished and the degree of in- and out-of-plane orientation can be determined using ATR-IR spectroscopy.

Table 1 Theoretically and experimentally determined dichroic ratios for all MOF films given in Fig. 5

	R (ν_{asymm}) predicted	R (ν_{asymm}) found[a]	R (ν_{symm}) predicted	R (ν_{asymm}) found[a]
x: random	∞	5.0	0.9	1.1
y: random		3.7		1.1
z‖[001]				
x: random	0.9	1.0	2	2.0
y: random		0.9		2.0
z‖[010]				
x‖[100]	0	0.2	∞	5.5
y‖[001]		0.3		5.0
z‖[010]				

[a] Top and bottom values correspond to $Cu_2(BDC)_2DABCO$ and $Cu_2(1,4\text{-}NDC)_2DABCO$, respectively.

Initial orientation of MOFs prepared *via* layer-by-layer deposition

So far, MOF films obtained from $Cu(OH)_2$ have been discussed, which have film thicknesses of 300–1200 nm (see Table S1 in ESI† for all films). The high thickness of the films allowed analysis in transmission and showed great absorbance values of up to 1 A.U. for spectra obtained in ATR configuration. The high sensitivity of the multibounce ATR crystals allows studying even thinner films as obtained by LbL synthesis. These films typically require a high number of deposited layers, typically >40 layers, to reach sufficient material enabling the characterization with laboratory XRD equipment. We studied the initial orientation of CuBDC, $Cu_2(BDC)_2DABCO$ and $Cu_2(1,4\text{-}NDC)_2DABCO$ films prepared on Si ATR crystals *via* LbL deposition methods (see ESI† for synthesis). In contrast to standard LbL deposition on SAM-modified Au surfaces, which would impede IR spectroscopy due to the high absorbance of Au, we followed a recent report on LbL on blank Si surfaces.[46] The LbL method yields MOF film oriented in z-direction but without in-plane orientation. Therefore, the obtained XRD patterns of all films for >10

layers for 3D MOFs and >40 layers for CuBDC were in accordance with the XRD patterns obtained from films grown from randomly oriented $Cu(OH)_2$ nanobelts (see Fig. S12 in ESI† for XRD data) and with patterns reported in literature.[30,47]

Polarization-dependent ATR spectra of CuBDC, $Cu_2(BDC)_2$-DABCO and $Cu_2(1,4\text{-NDC})_2$DABCO with 3 and 10 layers, respectively, are given in Fig. 6. While due to the low film thickness of the films with three layers, no reflections in the XRD patterns were detected using standard integration times, the polarization dependence of the $\nu_{asymm}(COO^-)$ is clearly visible for the 3D MOFs films. Spectra of CuBDC after 3 and 10 layer deposition are identical with the spectra of CuBDC films from random $Cu(OH)_2$. $Cu_2(BDC)_2$DABCO fits the structure of the film with [001] preferred OOP orientation without in-plane orientation: the $\nu_{asymm}(COO^-)$ band shows strong polarization dependence, as its transition dipole moment is aligned in z-direction, thus, this band is only visible in the p-polarized spectrum. Free rotation around the z-direction yield identical absorbance values for the $\nu_{symm}(COO^-)$ band. The $\nu_{asymm}(COO^-)$ bands allow to determine the degree of out-of-plane orientation ($F_{IR}(\nu_{asymm}(COO^-)) = F_{IR,OOP}$) according to eqn (2) to be 0.95 and 0.97 for 3 and 10 layers, respectively. A similar behavior was found for $Cu_2(1,4\text{-NDC})_2$DABCO for three deposited layers. However, the polarization-dependent spectra of the film with 10 layers show an increased absorbance for the p-polarized spectrum for all bands ($F_{IR,OOP} = 0.70$ and 0.57 for 3 and 10 layers, respectively). This indicates that the preferential order in z-direction of the $Cu_2(1,4\text{-NDC})_2$DABCO MOF decreases with increasing the number of deposition cycles. Although being less ordered, a dichroic ratio of $R = 2$ (for isotropic materials) is not observed. We attribute the deviation from $R = 2$ to the low film thickness that is known to decrease the field amplitude of E_z and thus the dichroic ratio for thin films converges to 1 for a film thickness of 0.[48] Given these results, polarization-dependent ATR spectroscopy allows for quick inspection and in-depth investigations of the orientation of MOF ultrathin films that are otherwise only accessible with long integration times or in synchrotron facilities.

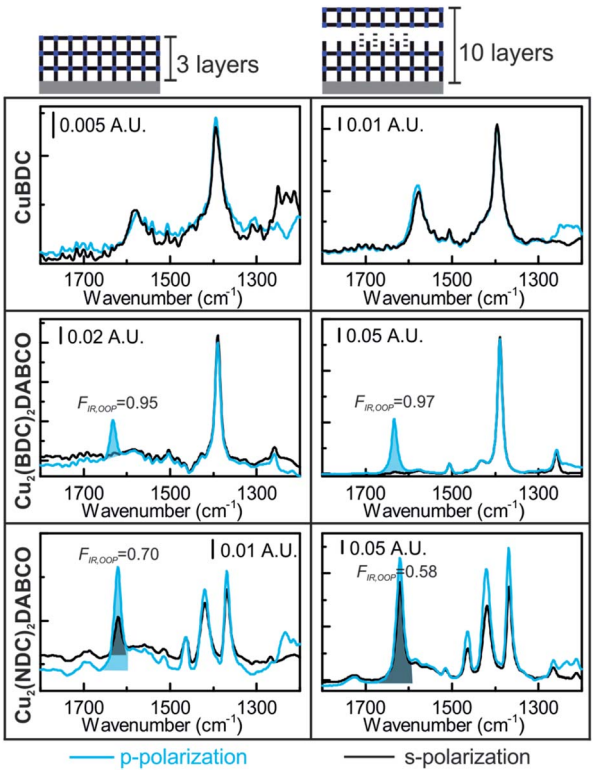

Fig. 6 Polarization-dependent ATR-IR spectra of MOF films prepared with the layer-by-layer method with 3 and 10 layers. The $\nu_{asymm}(COO^-)$ band of both 3D MOFs, $Cu_2(BDC)_2$DABCO and $Cu_2(1,4\text{-NDC})_2$DABCO, shows strong polarization dependence, which allows to calculate the degree of out-of-plane orientation from the band areas. Background = blank Si ATR crystal.

Orientation of aromatic linkers in MOF films

So far, the carboxylate vibrations have been used to study the orientation of the MOF film. By analyzing the vibrational modes of the aromatic rings in the MOF linkers, their orientation can be investigated as well. The skeletal ring vibrations of aromatic compounds are located between 1400 cm^{-1} and 1600 cm^{-1} with a transition dipole moment in-plane of the ring and perpendicular to the 1,4-C–C-axis (compare Fig. 7). Furthermore, the out-of-plane vibration of 1,4-substituted benzenes is found at 805 cm^{-1}.[49] We determined the direction of the transition dipole moments from a model compound using DFT calculations (see ESI† for details and Fig. 7A for orientation). The skeletal ring vibration is located at 1506 cm^{-1} for BDC. The film without in-plane orientation shows no polarization dependence because of the free rotation of the MOF film around the z-axis. In contrast, a strong polarization dependence is observed for three-dimensionally oriented $Cu_2(BDC)_2$DABCO films (see Fig. 5). The dichroic ratio $A_{\parallel}/A_{\perp}$ of the band at 1506 cm^{-1} was calculated for aligned and random MOFs films with [010] preferred OOP orientation and yielded 2 and 7.3, respectively. These ratios are almost identical to the $A_{\parallel}/A_{\perp}$ values of 2.1 and 6.4 found for the $\nu_{symm}(COO^-)$ band that has its transition dipole moment in the same direction. Based on this fact, we conclude that the aromatic ring is oriented perpendicular to its carboxylate plane (a–b lattice plane) as shown in Fig. 7B.

This finding was further verified in polarization dependent IR transmission spectra of the out-of-plane vibration at 798 cm^{-1}, which has its dipole moment oriented in y-direction and perpendicular to the band at 1506 cm^{-1}. Strong absorbance of the Si-ATR crystal at wavenumber <1000 cm^{-1} prevents measurements in ATR configuration. With a single path through the substrate in transmission configuration, however, the vibrational modes around 800 cm^{-1} can be analyzed (see Fig. S14 in ESI† for spectra). The band at 798 cm^{-1} shows high absorbance in the s-polarized spectrum, which is in line with the dipole assignment for an aromatic ring oriented perpendicular to the carboxylate plane.

Here, IR spectroscopy provides for the first time information on the linker orientation in $Cu_2(BDC)_2$DABCO, which is not accessible with XRD measurements as the rotation of the aromatic linker causes no change in the MOF patterns (compare

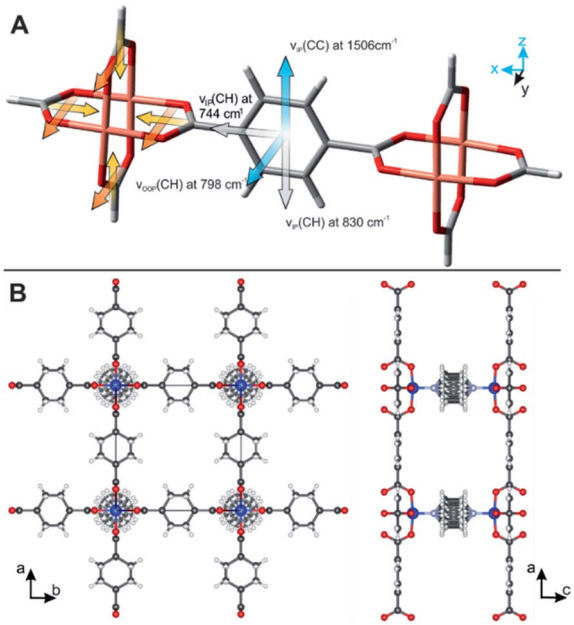

Fig. 7 (A) Illustration of the transition dipole moments for the aromatic vibrations found in the BDC linker. (B) Crystal structure of Cu_2(-BDC)$_2$DABCO with the proposed aromatic linker orientation perpendicular to the carboxylate plane.

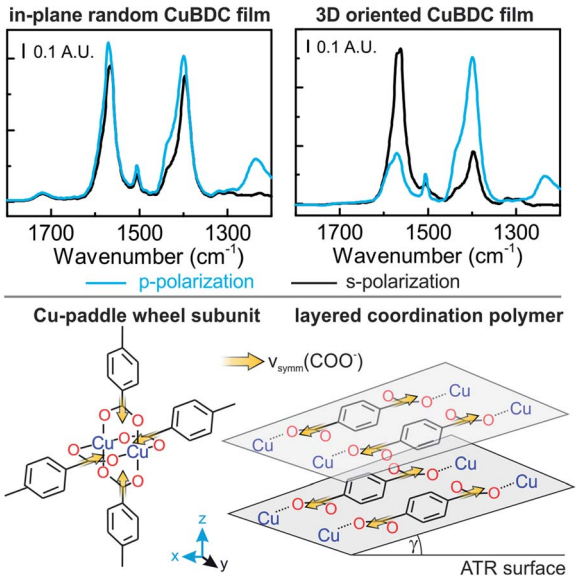

Fig. 8 (Top) Polarization-dependent ATR spectra of CuBDC prepared from random and aligned $Cu(OH)_2$. Background spectrum = blank Si ATR crystal. (Bottom) Cu-paddle wheel subunit found in 2D MOFs and BDC linker alignment in a layered coordination polymer. The transition dipole moment of the $\nu_{symm}(COO^-)$ bands are indicated by yellow arrows.

calculated patterns for crystal structures with different linker orientation in Fig. S16 in ESI†).

In contrast to $Cu_2(BDC)_2DABCO$, the aromatic linker vibration at 1515 cm^{-1} of $Cu_2(1,4\text{-NDC})_2DABCO$ shows no polarization dependence in the ATR spectra (compare Fig. 5). However, a strong polarization dependence, identical to $Cu_2(BDC)_2$-DABCO, is found for the out-of-plane vibrations in the region around of 800 cm^{-1} for the aligned MOF film (compare spectra in Fig. S17 in ESI†). Although this confirms a preferential orientation of the aromatic linkers with similar linker orientation as found in the $Cu_2(BDC)_2DABCO$, the polarization dependence is less pronounced. This is most likely due to the fact that the 1,4-NDC linker can either rotate freely as it has been suggested for coordination polymers,[50] or because the aromatic ring is not oriented parallel or perpendicular to the Cu-paddle wheel plane and is oriented under an angle of 48° as found in the reported crystal structure.[51]

Structure of CuBDC

The in-plane orientation of CuBDC films synthesized from the oriented $Cu(OH)_2$ nanobelts was confirmed by XRD patterns and transmission IR spectra, as shown in Fig. 1. Although the $\nu_{asymm}(COO^-)$ band showed good correlation with φ scan data of XRD investigations, $F_{IR}(\nu_{symm}(COO^-))$ showed deviations from F_{XRD}. In order to investigate this cause in more detail, polarization-dependent ATR spectra of CuBDC films were collected to investigate the three-dimensional molecular orientation. While the spectra of the three-dimensionally oriented CuBDC film only allow for retrieving the degree of orientation, information of the molecular orientation can be gained from the CuBDC film without in-plane orientation prepared from random $Cu(OH)_2$ (compare Fig. 8): equal absorbance values for p- and s-polarized light were expected for the $\nu_{asymm}(COO^-)$ band and were found in the spectra ($R = 0.3/0.33 = 0.9$, found: 1.2). Although the $\nu_{symm}(COO^-)$ band was expected to exhibit a dichroic ratio of 2, $R = 1.15$ was observed. The dichroic ratio from IR spectra in ATR and transmission configuration of the $\nu_{symm}(COO^-)$ band suggests that the BDC linkers are to a great extent oriented parallel to the surface; unlike in the Cu paddle wheel structure with 50% of the carboxylate bands in perpendicular orientation. The XRD pattern of CuBDC shown in Fig. 1 can be attributed to the structure consisting of Cu paddle wheels linked by four BDC with *P*4 symmetry, as found in previous reports.[38] However, in general, there is less certainty in identifying the structure when there are few reflections in XRD patterns. It is also difficult to identify the local coordination structure in MOF by XRD. Our IR results indicate a different CuBDC structure constituting of different coordination bonds between Cu and carboxylic acids, similar to the structures observed in copper(II) terephthalate and copper(II) hydroxy-terephthalate coordination polymers (see Fig. S18 and S19 in ESI†).[52–55]

We considered these structures and tested them against the IR spectra: for linkers parallel to the surface ($\gamma = 0°$), both carboxylate vibrations would show no contribution in *z*-direction. Thus, the transmission spectra and the ATR spectra would be identical. However, the band ratio $\nu_{symm}(COO^-)/\nu_{asymm}$(-$COO^-$) of 0.77 for transmission spectra of random CuBDC compared to 0.92 for the same film in ATR configuration suggests that the $\nu_{symm}(COO^-)$ band has a component in *z*-direction, which is not accessible in transmission. From this

ratio, a percentage of 19% of linkers aligned perpendicular to the surface was derived. The fraction of CuBDC with linkers oriented perpendicular to the surface causes a 100 reflection in the out-of-plane XRD pattern at $2\theta = \sim 8.2°$, while the parallel oriented fraction leads to the same reflection in the in-plane pattern. Typically, the occurrence of this reflection in both XRD configurations is used to confirm the presence of the Cu paddle wheel subunit connected by BDC linkers, and thus, the 2D MOF structure. Since XRD patterns obtained from different configurations cannot be compared quantitatively, we cannot assign the 100 reflection in the OOP pattern unambiguously to either the fraction of 19% of misaligned crystallites or the presence of a 2D MOF structure. However, the usually low porosity observed for CuBDC[39] and the position of the COO^- bands in the IR spectrum further point towards a more densely packed layered structure. While in 3D MOFs the $\nu_{asymm}(COO^-)$ band is located between 1610–1640 cm^{-1},[30] this band is located at 1570 cm^{-1} for CuBDC, which is the same position as reported for layered structures.[25] Therefore, a different copper carboxylate connectivity, as reported for the layered structure, can be assumed in the CuBDC structure. Note that the methodology to calculate the degree of in-plane orientation F_{IR} based on IR spectroscopy in transmission, as presented in the previous section, is still applicable for this structure: F_{IR} derived from $\nu_{asymm}(COO^-)$ is not affected by the tilting as its direction of the transition dipole moment is still in x–y plane. In summary, polarization-dependent IR spectroscopy provided information of the types of coordination bonds and their three-dimensional orientations in the CuBDC structure, which are difficult to reveal by XRD. It can be expected that the combination of XRD and polarization-dependent IR spectroscopy will contribute significantly to the complete clarification of the real structure of other coordination polymers and MOFs with unknown structures.

Conclusion

The orientation of 2D and 3D MOF films was studied using polarization dependent IR spectroscopy. MOF films were prepared on Si substrates and Si ATR crystals by layer-by-layer synthesis and from aligned $Cu(OH)_2$ precursor films. Cu_2(-BDC)$_2$DABCO and Cu_2(1,4-NDC)$_2$DABCO served as model systems as their established synthesis allowed to easily adjust their crystallographic orientation.[21] However, we provide the theoretical underpinnings to extend the principle to MOFs with different subunits (compare eqn (7a) and (7b)). A new method to determine the degree of in-plane orientation of MOFs based on straight-forward IR transmission measurements was presented that bears comparison with conventional techniques based on XRD. The method is not suitable for investigations of ultrathin MOF films, as FTIR spectroscopy in transmission has a low sensitivity and the presented method thus relies on sufficient film thickness. In contrast, the high sensitivity of multibounce ATR crystals allowed us to study the orientation of the initial few layers of MOF films during LbL synthesis, usually requiring synchrotron irradiations or extensive integration times. We found a decrease in out-of-plane orientation with increasing number of layers only for Cu_2(1,4-NDC)$_2$DABCO, while Cu_2(-BDC)$_2$DABCO remains oriented. For the first time, experimental evidence of the organic linker alignment perpendicular to the carboxylate plane in Cu_2(BDC)$_2$DABCO films was derived from the dichroic ratio of the ring vibrations of the aromatic linker. Information on the linker orientation is essential for applications that rely on mass transport along the pores that might be hindered by linkers extending into the pore channel. Finally, inexplicable polarization dependent IR spectra of the 2D MOF CuBDC made us revisit its structure. In contrast to data from XRD, IR crystallography revealed that the metal ions are not connected *via* a Cu-paddle wheel subunit as reported so far but in a layered structure.

Future work will combine the experimental setup with adsorption studies of probe molecules, similar to ref. 56 and 57. These would not just allow to investigate the orientation of the MOF itself but the alignment of guest molecules during the adsorption process. Insights into the orientation and adsorption site of the probe molecules will deepen the understanding of interactions between adsorbent and adsorbate, which is key to exploit the full potential of MOF films.

The presented principles are not limited to MOF films but can be easily translated to other thin films, *e.g.* inorganic, organic and inorganic–organic hybrid thin films. For instance, the orientation of nanocrystal films based on heavy atoms can be easily studied by X-ray and electron diffraction. However, these nanocrystals are typically stabilized with organic ligands, which significantly influence the nanocrystal's properties. For organic ligands and the orientation of functional groups, diffraction techniques lack in sensitivity. In general, inorganic–organic composite materials account for the majority of nanomaterials with highly promising properties currently under intense investigations. Consequently, the potential of IR crystallography has yet to be fully exploited, allowing to fill the information gap left by diffraction techniques and giving access to key information of hybrid material structures.

Author contributions

B. B.: Design of methodology, MOF synthesis, curation, writing – original draft; K. I.: MOF synthesis; K. O.: validation, writing – review & editing, resources; M. T.: validation, resources, writing – review & editing, funding acquisition.

Conflicts of interest

There are no conflicts to declare.

Acknowledgements

The present work is partially supported by Grand-in-Aids from the Ministry of Education, Culture, Sports, Science and Technology (MEXT), administrated by Japan Society for the Promotion of Science (JSPS), and also by JST, PRESTO Grant Number JPMJPR19I3, Japan. B. B. acknowledges the support *via* JSPS Invitational Fellowships for Research in Japan (PE20025). K. O. acknowledges financial support from Izumi Science,

Technology Foundation and the Cooperative Research Program of Institute for Catalysis, Hokkaido University (21B1019). The authors thank Paolo Falcaro and Jakob Hayden for fruitful discussions.

Notes and references

1 H. Furukawa, K. E. Cordova, M. O'Keeffe and O. M. Yaghi, *Science*, 2013, **341**, 1230444.
2 Y. Cui, J. Zhang, H. He and G. Qian, *Chem. Soc. Rev.*, 2018, **47**, 5740–5785.
3 V. Bon, *Curr. Opin. Green Sustain. Chem.*, 2017, **4**, 44–49.
4 H. Wang, Q. L. Zhu, R. Zou and Q. Xu, *Chem*, 2017, **2**, 52–80.
5 V. Pascanu, G. González Miera, A. K. Inge and B. Martín-Matute, *J. Am. Chem. Soc.*, 2019, **141**, 7223–7234.
6 D. Yang and B. C. Gates, *ACS Catal.*, 2019, **9**, 1779–1798.
7 Y. He, F. Chen, B. Li, G. Qian, W. Zhou and B. Chen, *Coord. Chem. Rev.*, 2018, **373**, 167–198.
8 H. Li, K. Wang, Y. Sun, C. T. Lollar, J. Li and H. C. Zhou, *Mater. Today*, 2018, **21**, 108–121.
9 Z. Liao, T. Xia, E. Yu and Y. Cui, *Crystals*, 2018, **8**, 338.
10 H. Y. Li, S. N. Zhao, S. Q. Zang and J. Li, *Chem. Soc. Rev.*, 2020, **49**, 6364–6401.
11 D. J. Wales, J. Grand, V. P. Ting, R. D. Burke, K. J. Edler, C. R. Bowen, S. Mintova and A. D. Burrows, *Chem. Soc. Rev.*, 2015, **44**, 4290–4321.
12 Y. Zhang and C. H. Chang, *Processes*, 2020, **8**, 377.
13 Z. Fu and G. Xu, *Chem. Rec.*, 2017, **17**, 518–534.
14 X. Mu, W. Wang, C. Sun, J. Wang, C. Wang and M. Knez, *Adv. Mater. Interfaces*, 2021, 2002151.
15 O. Shekhah, H. Wang, S. Kowarik, F. Schreiber, M. Paulus, M. Tolan, C. Sternemann, F. Evers, D. Zacher, R. A. Fischer and C. Wöll, *J. Am. Chem. Soc.*, 2007, **129**, 15118–15119.
16 C. L. Ruiz-Zambrana, M. Malankowska and J. Coronas, *Dalton Trans.*, 2020, **49**, 15139–15148.
17 J. L. Zhuang, A. Terfort and C. Wöll, *Coord. Chem. Rev.*, 2016, **307**, 391–424.
18 C. Crivello, S. Sevim, O. Graniel, C. Franco, S. Pane, J. Puigmarti-Luis and D. Munoz-Rojas, *Mater. Horiz.*, 2021, **8**, 168–178.
19 J. L. Zhuang, M. Kind, C. M. Grytz, F. Farr, M. Diefenbach, S. Tussupbayev, M. C. Holthausen and A. Terfort, *J. Am. Chem. Soc.*, 2015, **137**, 8237–8243.
20 P. Falcaro, K. Okada, T. Hara, K. Ikigaki, Y. Tokudome, A. W. Thornton, A. J. Hill, T. Williams, C. Doonan and M. Takahashi, *Nat. Mater.*, 2017, **16**, 342–348.
21 K. Okada, M. Nakanishi, K. Ikigaki, Y. Tokudome, P. Falcaro, C. J. Doonan and M. Takahashi, *Chem. Sci.*, 2020, **11**, 8005–8012.
22 K. Ikigaki, K. Okada, Y. Tokudome, T. Toyao, P. Falcaro, C. J. Doonan and M. Takahashi, *Angew. Chem., Int. Ed.*, 2019, **58**, 6886–6890.
23 F. M. Hoffmann, *Surf. Sci. Rep.*, 1983, **3**, 107–192.
24 C. Yang and C. Wöll, *Adv. Phys.: X*, 2017, **2**, 373–408.
25 G. Delen, Z. Ristanović, L. D. B. Mandemaker and B. M. Weckhuysen, *Chem.–Eur. J.*, 2018, **24**, 187–195.
26 K. Müller, N. Vankova, L. Schöttner, T. Heine and L. Heinke, *Chem. Sci.*, 2019, **10**, 153–160.
27 P. St. Petkov, G. N. Vayssilov, J. Liu, O. Shekhah, Y. Wang, C. Wöll and T. Heine, *ChemPhysChem*, 2012, **13**, 2025–2029.
28 P. R. Griffiths and J. A. de Hasseth, *Fourier Transform Infrared Spectrometry (FTIR)*, Wiley-Interscience, 2015, vol. 222.
29 R. G. Greenler, *J. Chem. Phys.*, 1966, **44**, 310–315.
30 X. J. Yu, Y. M. Xian, C. Wang, H. L. Mao, M. Kind, T. Abu-Husein, Z. Chen, S. B. Zhu, B. Ren, A. Terfort and J. L. Zhuang, *J. Am. Chem. Soc.*, 2019, **141**, 18984–18993.
31 M. Köberl, M. Cokoja, W. A. Herrmann and F. E. Kühn, *Dalton Trans.*, 2011, **40**, 6834–6859.
32 S. C. Park, Y. Liang and H. S. Lee, *Macromolecules*, 2004, **37**, 5607–5614.
33 L. Bokobza, *Polymers*, 2019, **11**, 1159.
34 S. K. Mallapragada and B. Narasimhan, in *Encyclopedia of Analytical Chemistry*, John Wiley & Sons, Ltd, Chichester, UK, 2006.
35 J. Heberle and T. Gensch, *Nat. Struct. Biol.*, 2001, **8**, 195–197.
36 J. T. Sage, *Appl. Spectrosc.*, 1997, **51**, 568–573.
37 R. D. B. Fraser, *J. Chem. Phys.*, 1953, **21**, 1511–1515.
38 J. Liu, B. Lukose, O. Shekhah, H. K. Arslan, P. Weidler, H. Gliemann, S. Bräse, S. Grosjean, A. Godt, X. Feng, K. Müllen, I. B. Magdau, T. Heine and C. Wöll, *Sci. Rep.*, 2012, **2**, 1–5.
39 Z. Wang, K. Rodewald, R. Medishetty, B. Rieger and R. A. Fischer, *Cryst. Growth Des.*, 2018, **18**, 7451–7459.
40 *Polymer Morphology: Principles, Characterization, and Processing*, ed. Q. Guo, Wiley, 2016.
41 K. I. Hadjiivanov, D. A. Panayotov, M. Y. Mihaylov, E. Z. Ivanova, K. K. Chakarova, S. M. Andonova and N. L. Drenchev, *Chem. Rev.*, 2021, **121**(3), 1286–1424.
42 V. I. Kovalenko, A. A. Akhmadiyarov, A. E. Vandyukov and A. R. Khamatgalimov, *J. Mol. Struct.*, 2012, **1028**, 134–140.
43 N. J. Harrick, *J. Opt. Soc. Am.*, 1965, **55**, 851.
44 U. P. Fringeli, *Chimia*, 1992, **46**, 200–214.
45 F. M. Mirabella, *Internal Reflection Spectroscopy: Theory and Applications*, Marcel Dekker, 1993.
46 B. D. McCarthy, T. Liseev, A. M. Beiler, K. L. Materna and S. Ott, *ACS Appl. Mater. Interfaces*, 2019, **11**, 38294–38302.
47 O. Shekhah, K. Hirai, H. Wang, H. Uehara, M. Kondo, S. Diring, D. Zacher, R. A. Fischer, O. Sakata, S. Kitagawa, S. Furukawa and C. Wöll, *Dalton Trans.*, 2011, **40**, 4954–4958.
48 E. Goormaghtigh, V. Raussens and J. M. Ruysschaert, *Biochim. Biophys. Acta, Rev. Biomembr.*, 1999, **1422**, 105–185.
49 G. Socrates, *Infrared and Raman Characteristic Group Frequencies: Tables and Charts*, Wiley, 3rd edn, 2004.
50 S. Horike, R. Matsuda, D. Tanaka, S. Matsubara, M. Mizuno, K. Endo and S. Kitagawa, *Angew. Chem., Int. Ed.*, 2006, **45**, 7226–7230.
51 S. Furukawa, K. Hirai, K. Nakagawa, Y. Takashima, R. Matsuda, T. Tsuruoka, M. Kondo, R. Haruki, D. Tanaka, H. Sakamoto, S. Shimomura, O. Sakata and S. Kitagawa, *Angew. Chem., Int. Ed.*, 2009, **48**, 1766–1770.
52 S. Abdelouhab, M. François, E. Elkaim and P. Rabu, *Solid State Sci.*, 2005, **7**, 227–232.

53 L. Deakin, A. M. Arif and J. S. Miller, *Inorg. Chem.*, 1999, **38**, 5072–5077.
54 T. Stassin, S. Rodríguez-Hermida, B. Schrode, A. J. Cruz, F. Carraro, D. Kravchenko, V. Creemers, I. Stassen, T. Hauffman, D. De Vos, P. Falcaro, R. Resel and R. Ameloot, *Chem. Commun.*, 2019, **55**, 10056–10059.
55 P. J. Kitson, R. J. Marshall, D. Long, R. S. Forgan and L. Cronin, *Angew. Chem., Int. Ed.*, 2014, **53**, 12723–12728.
56 B. Baumgartner, J. Hayden, J. Loizillon, S. Steinbacher, D. Grosso and B. Lendl, *Langmuir*, 2019, **35**(37), 11986–11994.
57 F. Bonino, C. Lamberti and S. Bordiga, in *The Chemistry of Metal-Organic Frameworks: Synthesis, Characterization, and Applications*, Wiley-VCH Verlag GmbH & Co. KGaA, 2016, pp. 657–690.

